Article

The Effects of a Varied Gold Shell Thickness on Iron Oxide Nanoparticle Cores in Magnetic Manipulation, T_1 and T_2 MRI Contrasting, and Magnetic Hyperthermia

Grace Brennan [iD]**, Silvia Bergamino, Martina Pescio, Syed A. M. Tofail and Christophe Silien ***

Department of Physics and Bernal Institute, University of Limerick, Limerick V94 T9PX, Ireland;
grace.brennan@ul.ie (G.B.); silviabergamino@gmail.com (S.B.); martina.pescio@gmail.com (M.P.);
tofail.syed@ul.ie (S.A.M.T.)
* Correspondence: christophe.silien@ul.ie

Abstract: Fe_3O_4–Au core–shell magnetic-plasmonic nanoparticles are expected to combine both magnetic and light responsivity into a single nanosystem, facilitating combined optical and magnetic-based nanotheranostic (therapeutic and diagnostic) applications, for example, photothermal therapy in conjunction with magnetic resonance imaging (MRI) imaging. To date, the effects of a plasmonic gold shell on an iron oxide nanoparticle core in magnetic-based applications remains largely unexplored. For this study, we quantified the efficacy of magnetic iron oxide cores with various gold shell thicknesses in a number of popular magnetic-based nanotheranostic applications; these included magnetic sorting and targeting (quantifying magnetic manipulability and magnetophoresis), MRI contrasting (quantifying benchtop nuclear magnetic resonance (NMR)-based T_1 and T_2 relaxivity), and magnetic hyperthermia therapy (quantifying alternating magnetic-field heating). We observed a general decrease in magnetic response and efficacy with an increase of the gold shell thickness, and herein we discuss possible reasons for this reduction. The magnetophoresis speed of iron oxide nanoparticles coated with the thickest gold shell tested here (ca. 42 nm) was only ca. 1% of the non-coated bare magnetic nanoparticle, demonstrating reduced magnetic manipulability. The T_1 relaxivity, r_1, of the thick gold-shelled magnetic particle was ca. 22% of the purely magnetic counterpart, whereas the T_2 relaxivity, r_2, was 42%, indicating a reduced MRI contrasting. Lastly, the magnetic hyperthermia heating efficiency (intrinsic loss power parameter) was reduced to ca. 14% for the thickest gold shell. For all applications, the efficiency decayed exponentially with increased gold shell thickness; therefore, if the primary application of the nanostructure is magnetic-based, this work suggests that it is preferable to use a thinner gold shell or higher levels of stimuli to compensate for losses associated with the addition of the gold shell. Moreover, as thinner gold shells have better magnetic properties, have previously demonstrated superior optical properties, and are more economical than thick gold shells, it can be said that "less is more".

Keywords: magnetic-plasmonic nanoparticles; nuclear magnetic resonance; magnetic hyperthermia; magnetic drug delivery; gold shell; magnetic manipulation; nanotheranostics

---

1. Introduction

Inorganic nanomaterials such as gadolinium [1], iron oxide [2], silica [3], and gold [4] are becoming increasingly popular in nanotheranostic applications (combined therapeutics and diagnostics), particularly as imaging agents, drug deliverers, and hyperthermia agents. It is hypothesized that combining materials into a single nanoplatform strengthens the physical properties of the nanosystem.

One such example is the combination of a magnetic and plasmonic material into a single hybrid nanostructure. Ideally, this magnetic-plasmonic nanoparticle will maintain the physical properties of each material when combined in the bi-functional nanomaterial. A plasmonic gold shell facilitates a number of optical-based applications, including surface-enhanced Raman scattering (SERS) [5], photothermal activity [6], and optical imaging contrast [7]; and these applications could be combined with magnetic-based applications if a magnetic core is used. For this study, we measured how a gold shell grown on a magnetite core affects the nanoparticle efficacy in various magnetic-based nanotherapeutic applications to understand the implications of magnetic-plasmonic nanoparticle hybridization. We found that, as prepared, the core–shell nanoparticle remains meaningfully efficient in magnetic-based applications for gold thicknesses of approximately ≤4 nm with iron oxide cores of ca. 20 nm.

Magnetic nanomaterials are at the forefront of inorganic nanotheranostics, particularly in diagnostics as contrast agents in nuclear magnetic resonance (NMR)-based applications, including magnetic resonance imaging (MRI) [8] and NMR-based biosensing [9], and in therapeutics as drug delivery [10,11] and hyperthermia agents [12]. The ability to manipulate or interact with material at the nanoscale with external stimuli is of utmost interest [13]. Magnetic nanomaterials may be manipulated by an external magnetic field, facilitating magnetic flux-driven drug delivery [10] for therapeutics, and magnetic separation of cells or blood [14] for diagnostics. Many types of magnetic nanoparticles exist, but superparamagnetic iron oxide (magnetite) nanoparticles are arguably the most prevalent in nanotheranostics [15]. Superparamagnetism is a type of magnetism that exists in nanoscale single magnetic domain ferri- or ferromagnetic materials. Superparamagnetic nanoparticles have two stable antiparallel orientations of the magnetic moment, with an energy barrier separating these orientations. In the absence of an external magnetic field and at temperatures where the energy barrier is less than the thermal fluctuation energy, the magnetic moment regularly flips direction leading to a net magnetization averaged to zero. In other words, superparamagnetic nanoparticles exhibit a net zero magnetic moment at certain temperatures in the absence of a magnetic field. However, when a magnetic field is applied, the magnetic moments align with the field, acting like a paramagnet but with higher magnetic susceptibility. Non-superparamagnetic magnetic nanoparticles experience strong interparticle magnetic forces in the absence of an external field that leads to aggregation. By contrast, superparamagnetic nanoparticles do not experience these strong interparticle magnetic forces in the absence of a magnetic field, and thus may be colloidally stable, a big advantage in many applications.

Along with superparamagnetic iron oxide nanoparticles, plasmonic nanoparticles are popular in the field of nanotheranostics [16–18]. A plasmon is a collective oscillation of the local electron density of a material; near optical resonance, this local electron density coherently oscillates with incident electromagnetic (light) excitation. This leads to enhanced optical absorption, scattering, and local electric field, which can be exploited in several applications including imaging [19,20] and sensing [21] and in drug delivery [22]. Furthermore, similar to magnetic nanomaterials, they are effective hyperthermia agents in plasmonic photothermal therapy [23]. When these plasmonic nanoparticles are excited by light near or at their optical resonance frequency, the mobile carriers dissipate their energy in the form of heat, which is then diffused into the surrounding area. Gold is typically chosen as the plasmonic material in bioapplications due to its stability, plasmon resonance located in the visible/near-infrared (NIR), and biocompatibility [24].

Many geometries of magnetic-plasmonic nanostructure exist, but to take advantage of the superior stability and biocompatibility of gold, the exterior should be gold, i.e., a core–shell structure. Magnetite–gold core–shell nanoparticles have also been used for photothermal activity [25], SERS enhancement [26], optical imaging contrast [27], interesting optical effects [28], enhanced Faraday rotation [29], and optical modulation in low-field magnetic relaxation [30] and have demonstrated good biocompatibility [31]. The gold shell in these reports varies dramatically, from thin or incomplete to thick gold shells. Ideally, such magnetic-plasmonic nanoparticles could be used in combined nanotheranostic applications, for example, photothermal therapy in combination with MRI imaging,

simultaneous optical imaging and magnetic hyperthermia, or magnetic separation combined with SERS. From our previous work [28], we found that thicker gold shells led to increased light scattering, and we would also expect decreased cytotoxicity [32] and circulation half-life [33] for this nanostructure. Meanwhile, thin-to-moderate gold shells facilitated spectrally selective photothermal activity due to the emergence of a spectral drift [28]. For this study, we explored the effects of the plasmonic gold shell in three notable magnetic-based applications, by comparing five different stages of magnetic-plasmonic nanoparticle with varied gold shell thickness. The three popular nanotheranostic applications considered were magnetic separation and targeting ability (by quantifying magnetophoresis), T_1 and T_2 MRI contrasting (by quantifying NMR relaxivity), and magnetic hyperthermia activity (by monitoring the heat generation in an alternating magnetic field).

2. Materials and Methods

2.1. Synthesis of Multistage Magnetic-Plasmonic Nanoparticles

First, 20.5 ± 1.3 nm diameter commercial oleic acid-capped iron oxide nanoparticles (Ocean NanoTech, San Diego, CA, USA) were amine functionalized by ligand exchange using (3-aminopropyl) triethoxysilane (APTES) and using a protocol modified from [34], to aid further functionalization and improved biocompatibility [35] (denoted O, black in graphs). Next, tetrakis(hydroxymethyl) phosphonium chloride (THPC)-reduced gold nanoseeds prepared by the Duff method [36] were grafted onto the iron oxide core giving a core–satellite or seeded stage (Os, red). The gold-seeded iron oxide nanoparticles were then subjected to three iterative gold reductions using a gold-plating solution and formaldehyde reduction modified from [37], yielding three further stages of gold growth called R1 (green), R2 (blue), and R3 (orange) throughout, and had a diameter determined by TEM of 28.5 ± 2.2, 42.1 ± 10.3, and 103.7 ± 16.9 nm, respectively. To read further details about the synthesis of these multistage magnetic-plasmonic nanostructures and see transmission electron micrographs of the various stages, please see our earlier work in [24]. To aid the comparison between gold-coated stages and uncoated iron oxide, the mass of iron oxide (i.e., the number of nanoparticles) was kept constant in this work.

2.2. Magnetophoresis

To conduct optical tracking of magnetophoresis, a deuterium–halogen UV–VIS–NIR light source (DH2000-BAL, Ocean Optics, Orlando, FL, USA) using only halogen as the light source was passed through a quartz cuvette (CV10Q3500, Thorlabs, Newton, NJ, USA) containing the suspended nanoparticles. The transmitted light was focused onto a flame spectrometer (Ocean Optics), which was paired with OceanView software (Version 1.6.7, Ocean Optics). The probed area was a cylindrical region in the cuvette with a 5 mm diameter and a 10 mm height, centered 70 mm above a magnet (neodymium, 10 mm × 10 mm × 10 mm). The magnet's distance-dependent magnetic flux density was measured using a gaussmeter. The extinction peak was monitored temporally, and a linear fit of the peak extinction is used to monitor magnetophoresis.

2.3. NMR T_1 and T_2 Relaxation Measurements

To conduct T_1 and T_2 measurements of the multistage magnetic-plasmonic nanostructures, a benchtop NMR (^{1}H Spinsolve 60 MHz, Magritek, Malvern, PA, USA) was used. The magnetic field strength was 1.5 Tesla, and the proton Larmor frequency was 60MHz. To track the effect of the gold shell on the magnetic nanoparticle relaxivity, the ^{1}H (water) peak at ≈4.8 ppm was monitored.

T_1 measurements were conducted using an inversion recovery pulse sequence, starting with the shortest inversion delay; a series of experiments were conducted with the inversion delay stepped linearly to the maximum inversion time. Two scans of 1.6 s acquisition time (8192 points, dwell time of 200 μs), repetition time of 7 s, and a varied inversion time of ≈5 s with 21 steps were taken for the T_1 measurements.

T_2 measurements were made using a Carr–Purcell–Meiboom–Gill (CPMG) pulse sequence, starting with the shortest echo time τ; a series of measurements were conducted where 180-degree pulses were stepped linearly, ending with the final (variable) echo time. Four scans with an acquisition time of 0.4 s (8192 points, 50 μs dwell time), 4 s repetition time, 20 steps with a CPMG echo time of 0.2 ms, and a varied final echo time of ≈2 s were taken for the T_2 measurements. The 90° pulse width was 7 ms for both measurements.

2.4. Magnetic Hyperthermia

In this research, a Flexitune induction heater (Radyne, Wokingham, UK) was used with a water-cooled homemade copper coil, generating a 100 mT alternating magnetic field, with a frequency of 20 kHz. Induction heaters are typically used to heat a conductive material by eddy currents. Induction heaters are simply AC passed through an inductor (e.g., coil), thus producing an alternating magnetic field, per Ampere's law. A calibrated A655sc (FLIR, Wilsonville, OR, USA) infrared camera was used to monitor the magnetic field-induced hyperthermal activity, noncontact. Aqueous solutions of the various stages of magnetic-plasmonic nanoparticles in an Eppendorf tube (Eppendorf, Hamburg, Germany) (at a fixed concentration of 0.2 mg/mL of iron oxide) were suspended inside the cooled copper coil (noncontact) using a plastic mount. It is important to note that these measurements were not conducted under adiabatic conditions (i.e., there was a loss to the environment) unlike many other magnetic hyperthermia measurements [38], which are thermally insulated.

3. Results

To determine whether a gold coating affects the efficacy of magnetic nanoparticles in various magnetic-based nanotheranostic applications, Fe_3O_4–Au nanoparticles were synthesized with various stages of gold growth (see Section 2.1 for details). An illustration of the various nanoparticle stages is shown in Figure 1.
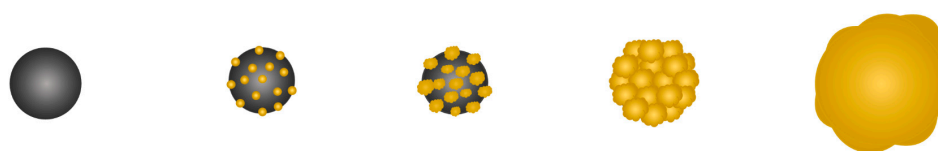
Iron Oxide (O)　Seeded (Os)　Plated (R1)　Popcorn (R2)　Continuous (R3)

Figure 1. Illustration of the various forms and thicknesses of magnetic-plasmonic nanoparticles studied for this paper. From left, the (3-aminopropyl) triethoxysilane (APTES) functionalized iron oxide (Fe_3O_4), called O throughout. Next, the Fe_3O_4 nanoparticles functionalized with gold seeds, Os. Middle, the Fe_3O_4–Au gold-plated nanoparticle after one gold reduction, R1. R2 is the magnetic-plasmonic nanoparticle after two gold reductions and, lastly, R3, after three gold reductions. Reproduced with permission from [28]; Copyright The Royal Society of Chemistry, 2020.

3.1. Magnetophoresis

Magnetic guidance or translation of magnetic (or hybrid magnetic) nanoparticles is vital in facilitating magnetic flux-driven drug delivery, magnetic cell or blood sorting, and magnetic field-guided therapy. Magnetic nanoparticles suspended in fluid travel toward the highest magnetic field gradient; this movement is called magnetophoresis. A higher magnetophoresis speed is preferable for most applications and has been achieved by using a stronger magnetic field gradient, higher nanoparticle magnetization or concentration, nanoparticle shape anisotropy [39], and surface charge [40]. Considerable work in the magnetophoresis of various magnetic (and magnetic-plasmonic) structures has been carried out [41–43]. Furthermore, the addition of a nonmagnetic silica [44,45] and polymer [43] shell has been shown to decrease the magnetophoretic mobility of magnetite nanoparticles.

Thus, if a polymer/silica shell affects the magnetophoresis, it is reasonable to hypothesize that a gold shell would also hamper this motion.

The magnetophoretic force, F_M, exerted on a magnetic particle by an external magnetic field is dependent on the magnetic particle volume, V_p, the magnetization of the nanoparticle, M_p, the permeability of free space, μ_0, and the magnetic field strength, H, at the particle location per [46,47]:

$$F_M = \mu_0 V_p M_p . \nabla H \tag{1}$$

Equation (1) is sufficient for non-interacting (noncooperative) high magnetic field gradient magnetophoresis. Drag and magnetic interaction forces should be considered in low magnetic field gradient magnetophoresis. For low magnetic field gradient (<100 T/m) magnetophoresis, as is the case here, typically magnetic particles cooperate by clustering together into chain-like structures while moving in the gradient, and this assembly accelerates the magnetophoresis transport [48,49]. This is likely due to the coupling of the individual magnetic moments of the nanoparticles into a new and larger effective magnetic moment. Furthermore, the drag force (friction) experienced by the assembled nanoparticles would be reduced per the slender-body theory [50]. Magnetic dipolar interaction forces that facilitate this magnetic assembly are increased when the nanoparticles are not colloidally stable and are in high concentrations (due to increased probability of proximity).

The magnetic saturation of Fe_3O_4–Au nanoparticles has been reported to be decreased compared to uncoated Fe_3O_4 by varying degrees from ≈10% to 70% [51–56], likely a result of increased gold-to-iron oxide mass ratio and magnetic shielding by the diamagnetic gold shell [57–59]. This reduced magnetic saturation has also been reported for other materials with increased shell thickness, including gold shells on cobalt nanoparticles [60] and silica shells on FeNi nanoparticles [61]. On the contrary, there are reports of increased magnetic saturation with the addition of a gold shell on Fe_3O_4 [62,63], and the authors hypothesized that conduction electrons are trapped, which induces an orbital moment. A reduction of magnetic saturation reduces the value M_p can reach, thus leading to a reduction in the magnetic force causing the translation of the nanoparticles to the magnet. As the gold shell on the Fe_3O_4 core was associated with a reduced saturation, we anticipated a reduced magnetic force and magnetophoresis.

In this work, the magnetophoresis of the multistage magnetic-plasmonic nanoparticles was monitored by optical extinction, per the experimental schematic seen in Figure 2A. In this experiment, the concentration of iron oxide (and thus, the number of nanoparticles) was kept constant. Therefore, the volume of magnetic material is constant, but the percentage per particle varies with each stage (see Table 1). Collimated light is passed through the cuvette containing the nanoparticles, which is then focused onto a fiber spectrometer. A permanent magnet is placed below the cuvette, with a distance-dependent magnetic flux density seen in Figure 2B. The probed area is a cylindrical region in the cuvette with a 5 mm diameter and a 10 mm height, centered 70 mm above the magnet. As the nanoparticles migrate toward the magnet (due to magnetic forces) and leave the probe area, the optical extinction decreases. The peak optical extinction was tracked during magnetophoresis and a linear fit was added (see Figure 2C). Further experimental details are given in the experimental Section 2.1.

From Figure 2C and Table 1, increasing the gold shell thickness leads to a significantly longer time to magnetically separate, i.e., decreased speed of magnetophoresis. The iron oxide nanoparticles without any gold coating take approximately 12 min to migrate out of the probed area of the solution. With the addition of gold, the magnetic separation time increases, eventually reaching 1421 min for the thickest gold shell. Thus, thinner gold shells are likely preferable for applications that require reasonable responsivity to the external magnetic field. Alternatively, much larger magnetic field gradients would be required to use these thick gold-shelled nanoparticles in such applications. It is likely a combination of a reduced magnetic saturation and loss of cooperative behavior of the thickly gold-coated nanoparticles that leads to reduced magnetophoresis. Furthermore, an increased drag force would be experienced by larger nanoparticles.
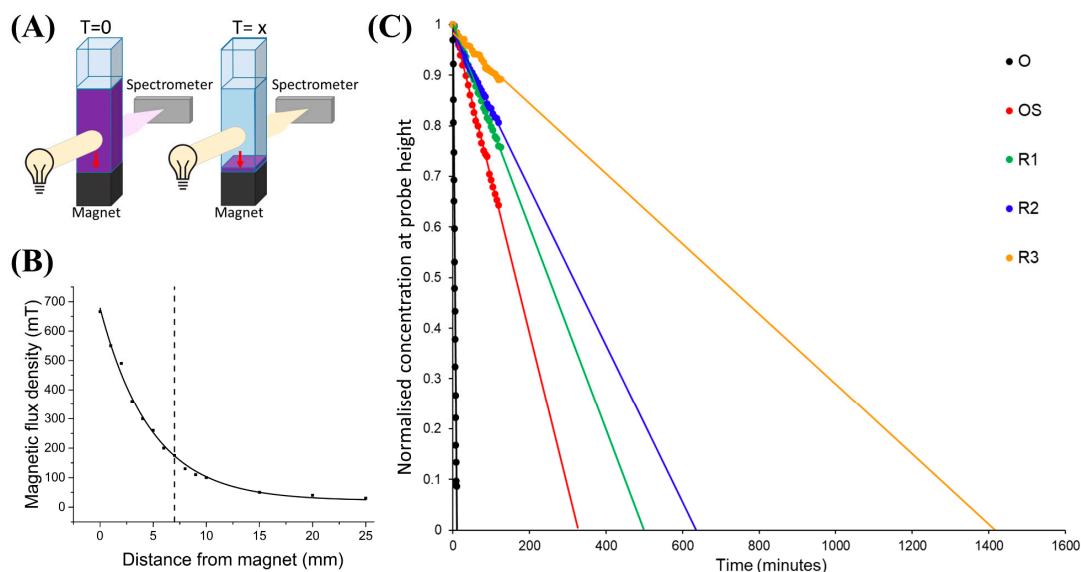
Figure 2. (**A**) The experimental setup to monitor the magnetophoretic behavior, using a white light source and spectrometer to monitor the diffusion of the nanoparticles to a permanent magnet. (**B**) The distance-dependent magnetic flux density of the permanent magnet used in this experiment, with the dashed line representing the probe height. (**C**) The magnetophoresis of the various stages of the magnetic-plasmonic nanoparticles. On the vertical axis, 1 represents the starting concentration of 20 µg/mL of Fe_3O_4. The data are extrapolated to estimate the time for total magnetophoresis out of the probed area.

Table 1. Overview of the key findings in this work for the five stages of nanoparticle. Percentages in brackets indicate the percentage as compared to the uncoated iron oxide nanoparticle.

Application	Fe_3O_4 (O)	Fe_3O_4 + Au Seeds (Os)	Fe_3O_4 + Thin Au Shell (R1)	Fe_3O_4 + Medium Au Shell (R2)	Fe_3O_4 + Thick Au Shell (R3)
Nanoparticle total diameter (nm) [28]	20.5 ± 1.3	O + ~3 nm seeds	28.5 ± 2.2	42.1 ± 10.3	103.7 ± 16.9
Shell thickness (nm) [28]	-	-	≈4	≈10.8	≈41.6
Zeta Potential (mV) [28]	0.0 ± 4.1	−10.0 ± 6.8	−27.3± 2.8	−22.4 ± 2.1	−22.1 ± 3.2
Magnetophoresis time (min)	12	326	498	636	1421
Magnetophoresis speed, v_{mag} (µm/s)	9.7	0.4 (4.1%)	0.2 (2.1%)	0.2 (2.1%)	0.1(1%)
T_1 relaxivity r_1 (mM/s)	0.9	0.7 (77.8%)	0.7 (77.8%)	0.3 (33.3%)	0.2 (22.2%)
T_2 relaxivity r_2 (mM/s)	32.7	21.9 (67%)	15.4 (47.1%)	15.1 (46.2%)	13.6 (41.6%)
Relaxivity ratio r_2/r_1	35.6	30.6 (86%)	23.3 (65.4%)	51.5 (144.7%)	55.5 (155.9%)
Max. temperature	3.4	2.1 (61.8%)	1.5 (44.1%)	0.3 (8.8%)	0.1 (2.9%)
Initial 60 s $\Delta T/\Delta t$ (m °C/s)	18.8	11.7 (62.2%)	6.2 (33%)	1.7 (9%)	1.3 (6.9%)
Specific power absorption (SPA) (W/g)	93.7	58.3 (62.2%)	30.9 (33%)	8.5 (9.1%)	6.5 (6.9%)
Intrinsic loss power parameter (ILP) (H m²/kg)	0.7	0.5 (71.4%)	0.2 (28.6%)	0.1 (14.3%)	0.1 (14.3%)

It should be noted that the surface charge of the nanoparticles may also affect the interaction between nanoparticles. Zeta potential measurements of the various stages of nanoparticle are given in Table 1, indicating good colloidal stability for R1, R2, and R3. Temperature and pH were constant throughout.

3.2. NMR/MRI Contrast Agent

MRI is a well-known non-ionizing technique that uses radio waves along with strong magnetic fields and gradients to conduct biological diagnostic imaging. MRI imaging is based on NMR principles, where certain atomic nuclei (typically hydrogen) undergo Larmor precession in a strong external magnetic field and, when the Larmor precession frequency of the nuclear magnet resonates with that of an incoming radio wave (RF pulse), energy is absorbed from the radio wave. Protons may align in two energy eigenstates, low and high energy, separated by a small splitting energy. At equilibrium, most protons reside in the low energy state (aligned with the external magnetic field) and a net polarization parallel to the external field. An incident resonant RF pulse may lead to the polarization

vector either tipping sideways (90° pulse) or reversing (180° pulse), and the protons come into phase with the pulse and one another (phase coherence). In response to the RF pulse, we may consider two relaxations to equilibrium, namely spin–lattice (also known as T_1 or longitudinal relaxation) and spin–spin (also known as T_2 or transverse relaxation). The recovery of the longitudinal magnetization relaxation (M_z) to its thermal equilibrium value ($M_{z,eq}$) is called the T_1 (spin–lattice) relaxation; as the T_1 relaxation is related to the redistribution of the spins to the low energy state (thermal equilibrium), energy is dissipated to the surroundings (lattice). T_2 relaxation involves the recovery of the equilibrium state dephased spin; therefore, the magnetization vector perpendicular (transverse) to the static magnetic field is considered, M_{xy}.

A downfall of MRI biological imaging is its low sensitivity. To combat low sensitivity, a contrast agent is commonly employed to selectively alter the relaxation time of the nuclei. As the magnetic relaxation of the nuclei varies with the square of the magnetic dipole moment, gadolinium (Gd^{3+}) with its seven unpaired electrons (high magnetic moment) is often used in chelated form to enhance MRI T_1 contrast. However, there are concerns regarding the safety of these gadolinium-based contrast agents [64]. Superparamagnetic nanoparticles have been proposed as an alternative, but rather mostly for T_2 image contrast.

In terms of MRI, a local reduction (shorter time) in either the T_1 relaxation (positive contrast) or T_2 relaxation (negative contrast) results in better image contrast. As the T_1 and T_2 times are concentration-dependent, we define relaxivities as a function of iron concentration, i.e., r_1 and r_2. The longitudinal relaxivity r_1 is said to depend on the molecular tumbling time, proton residence lifetime, and coordinating number, while the transverse relaxivity r_2 is proportional to the square of the magnetic nanoparticle radius and the magnetic saturation [65]. As the T_1 relaxation is associated with inner-sphere mechanisms (chemical energy exchange), superparamagnetic nanoparticles are instead more effective in T_2 applications.

In the case of magnetic core–nonmagnetic shell particles, the magnetic field experienced by the water protons (T_2) and the degree of chemical exchange (T_1) lessens with increased shell thickness. Furthermore, if the nanoparticles are aggregated or assembled, worse r_1 contrast due to reduced surface area and improved r_2 contrast owing to the coupling of the magnetic moments are expected [66]. A relaxivity ratio (r_2/r_1) is often used as another measure of contrast agent usefulness. An optimal negative contrast agent (T_2) would have a high r_2/r_1 ratio along with a high r_2 value. If this ratio is less than 5, the contrast would instead be considered a good candidate for a T_1 contrasting; if larger than 5, the agent may be more suitable for T_2 contrasting [67].

Several r_1 and r_2 relaxivities from the literature are presented in Table 2, as well as the values for the multistage magnetic-plasmonic structures from this work. Marangoni et al. [68] studied the T_1 relaxation of gold-core nanoparticles with a Gd(III) ion–silica layer, followed by a varied gold shell. Interestingly, T_1 contrast was better for the gold-based nanoparticles compared to the typical Gd-based chelating agents. They also found that contrast was optimal for a gold-seeded shell but was seen to decrease with additional gold growth. The authors suggest that the added mass from the shell decreases the tumbling rate, hence decreasing the relaxivity for the thicker shelled nanoparticles (worse contrast). Pinho et al. [69] studied the effect of silica shell thickness on the r_1 and r_2 relaxivities of γ-Fe_2O_3 (see Table 2 for details). The thickness of silica had a significant impact on both relaxivities, with increased shell thickness leading to a decrease in the relaxivity value (decreased contrast). Others show the decrease in r_1 [70] or decrease in both r_1 and r_2 [69,71] with the addition of a SiO_2 shell, similar to observations in this research with the addition of a gold shell. Moreover, Park et al. noted a reduced r_2 value for a diamagnetic avidin–biotin coating on Fe_3O_4 nanoparticles and attributed this to diamagnetic shielding effects [72]. Assembled magnetic structures were also seen to increase the r_2 relaxation [73]. In this work, benchtop ^{1}H NMR spectroscopy was used to monitor the effects of the multistage magnetic-plasmonic nanoparticles on the relaxation of the water associated peak at ca. 4.8 ppm. Information on the T_1 and T_2 measurement sequences can be found in the experimental Section 2.3.

Table 2. Relaxation properties of select examples from the literature, including SiO_2 shells of varied thicknesses and magnetically assembled structures. Relaxation properties of the magnetic-plasmonic nanoparticles studied in this work are shown in the last 5 lines.

Sample	r_1 (mM^{-1} s^{-1})	r_2 (mM^{-1} s^{-1})	r_2/r_1	Frequency (MHz)	Field (T)	Ref.
Fe_3O_4 (20 nm) @Au (5 nm)	-	181.35		-[1]	3	[56]
Fe_3O_4 (20 nm) @Au (5 nm) + PEG [2]		162.3		-	3	[56]
Fe_3O_4 9 nm + 1 nm SiO_2 shell		94		-	3	[70]
Fe_3O_4 9 nm + 5 nm SiO_2 shell		68		-	3	[70]
Fe_3O_4 9 nm + 10 nm SiO_2 shell		47		-	3	[70]
Fe_3O_4 9 nm + 13 nm SiO_2 shell		32		-	3	[70]
$Fe_2O_3 \approx$ 10 nm	32	≈228	≈7.1	r_1 $20r_2 \approx$500	r_1 $0.4r_2$ 11.7	[69]
$Fe_2O_3 \approx$10 nm + ≈2 nm SiO_2 shell	11.2	≈100	≈8.9	" [3]	"	[69]
$Fe_2O_3 \approx$10 nm + ≈8 nm SiO_2 shell	<2	≈64	≈32.0	"	"	[69]
$Fe_2O_3 \approx$10 nm + ≈15 nm SiO_2 shell	<2	≈47	≈23.5	"	"	[69]
$Fe_2O_3 \approx$10 nm + ≈20 nm SiO_2 shell	<2	≈38	≈19.0	"	"	[69]
$Fe_2O_3 \approx$10 nm + ≈28 nm SiO_2 shell	<2	≈23	≈11.5	"	"	[69]
$Fe_2O_3 \approx$10 nm + ≈52 nm SiO_2 shell	<2	≈15	≈7.5	"	"	[69]
$Fe_2O_3 \approx$10 nm + ≈67 nm SiO_2 shell	<2	≈13	≈6.5	"	"	[69]
Cluster core–shell Fe_3O_4 6 nm–APTES (≈96.6 nm total)	0.006	40.6	6766.7	300	7	[74]
Cluster core–shell Fe_3O_4 6 nm–GPTMS [4] (≈22.0 nm total)	0.026	14.4	553.8	300	7	[74]
Cluster core–shell Fe_3O_4 6 nm–TEOS [5] (≈66.6 nm total)	0.016	13.8	862.5	300	7	[74]
Fe_3O_4 (30 nm) with asymmetric surface chemistry (amine and thiol)	-	44.87		-	1.4	[73]
Nanochains of Fe_3O_4 (30 nm) with amine and thiol surface	-	101.05		-	1.4	[73]
Fe_3O_4 (11 nm)–CTAB [6]	31.25 (13.69)	81.37 (82.18)	2.6 (6.0)	20 (60)	0.47 (1.41)	[71]
Fe_3O_4 (12 nm) @mSiO_2 shell (50 nm total)	3.65 (1.31)	84.26 (92.13)	23.1 (70.3)	"	"	[71]
Fe_3O_4 (12 nm) @mSiO_2 shell (75 nm total)	2.13 (0.97)	79.93 (87.54)	37.5 (90.3)	"	"	[71]
Fe_3O_4 (12 nm) @mSiO_2 shell (95 nm total)	0.61 (0.31)	50.13 (55.44)	82.2 (178.8)	"	"	[71]
Fe_3O_4 (≈7.48 nm)	≈37	≈48	≈1.3	≈10	-	[75]
Fe_3O_4 (≈7.48 nm)–Au (5–8 nm) dimer	≈5	≈62	≈12.4	"	-	[75]
Au core (5–8 nm)–Fe_3O_4 shell (≈15.92 nm total)	≈27	≈41	≈1.5	"	-	[75]
Fe_3O_4 cluster (200 nm)	-	230.7		-	-	[55]
Fe_3O_4 cluster (200 nm) + 5 nm Au seeds	-	147.7		-	-	[55]
Fe_3O_4 cluster (200 nm) + 20 nm Au seeds	-	163.1		-	-	[55]
Fe_3O_4 cluster (200 nm) + 25 nm Au shell	-	158.2		-	-	[55]
Fe_3O_4	-	167		-	-	[76]
Fe_3O_4–Au (core–shell)	-	61.9		-	-	[76]
Fe_3O_4–Au (yolk–shell)	-	149.4		-	-	[76]
γ-Fe_2O_3 core–Au Shell ≈28.38 nm	≈8.82 (≈10.35)	≈4.04 (≈3.99)		- (532 nm light)	100 μT	[30]
20.5 ± 1.3 nm Fe_3O_4 (O)	0.92	32.70	35.55	60	1.5	This work
O + ≈3 nm Au seeds (Os)	0.72	21.94	30.56	"	"	"
O + ≈4 nm thick Au shell (R1)	0.66	15.43	23.27	"	"	"
O + ≈10.8 nm thick Au shell (R2)	0.29	15.06	51.48	"	"	"
O + ≈41.6 nm thick Au shell (R3)	0.24	13.58	55.48	"	"	"

[1] Unknown quantity. [2] Polyethylene glycol. [3] Ditto marks indicate repeated values. [4] (3-Glycidyloxypropyl)trimethoxysilane. [5] Tetraethyl orthosilicate. [6] Cetyltrimethylammonium bromide.

From the data presented in Figure 3 and Table 2, we can conclude that the added gold has a considerable impact on the relaxation properties of the iron oxide nanoparticles. Beginning with T_1 properties, the iron oxide nanoparticles (O) have a r_1 relaxivity of 0.92 mM^{-1} s^{-1}; this reduces with added gold to 0.24 mM^{-1} s^{-1} for the thick gold-shelled iron oxide nanoparticle (R3). In the case of with T_2 relaxation, there is also a reduction in the r_2 relaxivity, which is 32.70 mM^{-1} s^{-1} for the bare iron oxide (O) and 13.58 mM^{-1} s^{-1} for the iron oxide core with the thick gold shell (R3). Interestingly, the r_2/r_1 ratio is minimum for the iron oxide nanoparticle with a thin gold shell (23.27) and maximum for the thick gold-shelled iron oxide nanoparticle (55.48). This large ratio for the thick gold shell could suggest that this stage is a good candidate for T_2 imaging, but it is not paired with a high r_2 value. In summary, increasing the thickness of the gold shell reduces the relaxivity (increases the relaxation time) for both T_1 and T_2 MRI imaging, hence reducing the contrasting capability.
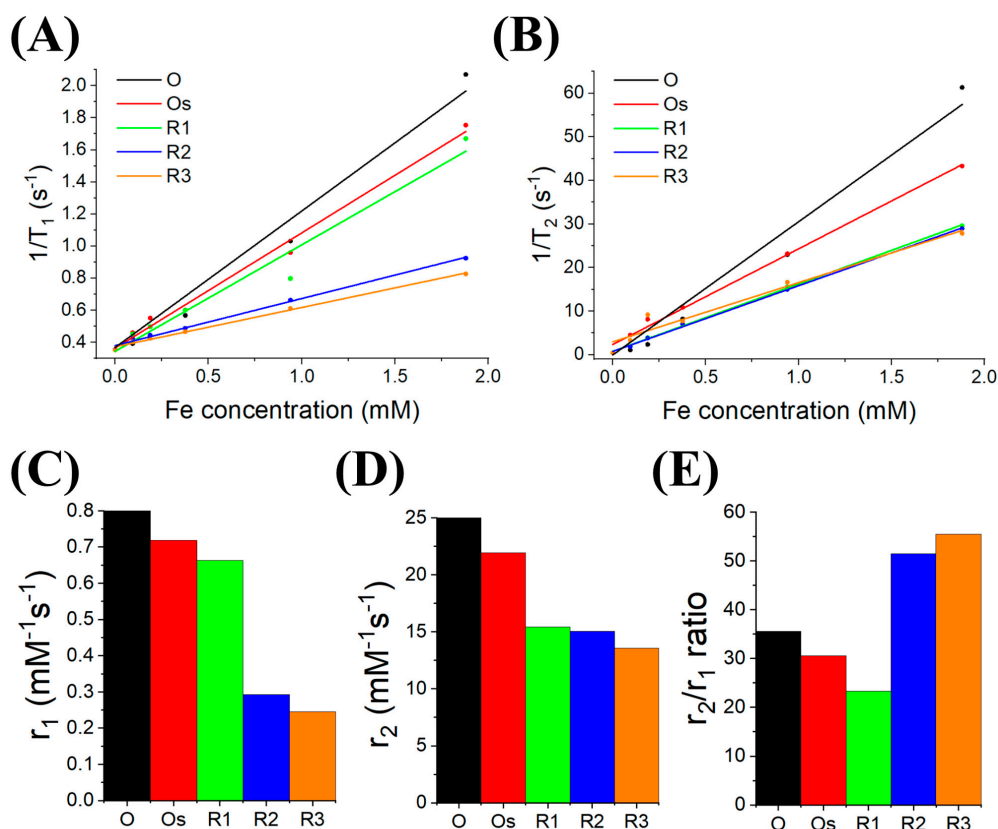
Figure 3. Nuclear magnetic resonance (NMR) of the various stages of magnetic-plasmonic nanostructures. (**A**) shows the T_1 relaxation time (s^{-1}) of the various nanostructures at different concentrations of iron (mM). (**B**) shows the graph of the T_2 relaxation time with varied concentrations of the multistage nanoparticles. (**C,D**) are bar graphs of the relaxivities r_1 and r_2, respectively. (**E**) shows the r_2/r_1 ratio of the magnetic-plasmonic nanostructures.

3.3. Magnetic Hyperthermia

Hyperthermia therapy is a medical treatment that involves raising the temperature of the body in an attempt to treat diseases such as cancer. Standard hyperthermia therapy may be delivered using infrared light, microwaves, or radiofrequency. Like with other cancer treatments, there are adverse effects when non-targeted tissue is affected, which can lead to blood clots or even cardiovascular issues [77]. The temperature to achieve cell death is debated, although most agree that 40–43 °C must be reached, about 3–6 °C above healthy body temperature (37 °C) [77]. It is important to note that such therapy is not a conventional therapy, and would rarely be used as the first choice for treatment due to non-selective heating. To combat issues with non-selective heating, nanoparticle agents have been proposed as a

technique for localizing the heat to targeted areas with minimal heating of the surrounding healthy tissue. One such nanoparticle agent is magnetic nanoparticles. Magnetic hyperthermia combines magnetic nanoparticles with an external high-frequency alternating magnetic field. To achieve selective heating, the nanoparticle should target the tumor site, using either passive or, preferably, active targeting techniques (using targeting ligands, magnetic field).

Typically, superparamagnetic nanoparticles are used as magnetic hyperthermia agents. Superparamagnetic nanoparticles flip to align their magnetic dipole to the external magnetic field orientation. When this magnetic field is alternating, and at a high frequency, these nanoparticles flip to orient with the field but lose power due to hysteresis, resulting in heat dissipation.

In an AC magnetic field, the magnetization of the nanoparticle may not be responsive enough to keep up with the AC frequency, resulting in a phase difference. This phase difference requires a complex magnetic susceptibility explanation. The concentration, size, and material of the nanomaterial impact the hyperthermia activity along with the field strength and frequency. Furthermore, magnetic assembly leads to higher hysteresis losses, thus increasing the heat generated [78]. A silica shell [79,80] and a polyphosphazene–gold shell [81] have also been shown to decrease magnetic hyperthermia activity.

To benchmark the heating efficiency of the magnetic-plasmonic nanoparticles, the specific power absorption (SPA) (W/g), also known as the specific absorption rate (SAR), is calculated per [82]. Furthermore, to account for the magnetic field strength and frequency used, the intrinsic loss power parameter (ILP) (H m^2 kg^{-1}) is calculated per [82].

From Figure 4 and Table 1, we can deduce that the addition of gold leads to a reduction in the magnetic hyperthermia activity. As previously discussed, it is likely that with the addition of gold there is a reduction of interparticle assembly as this formation is linked closely with an increased magnetic hyperthermia activity. The heating efficiency of commercial magnetic colloids has been reported to be between 0.15 and 3.12 nH m^2/kg Fe [12]. Therefore, the magnetic-plasmonic nanoparticles in this study are comparable until thicker gold shells are added (R2 and R3).
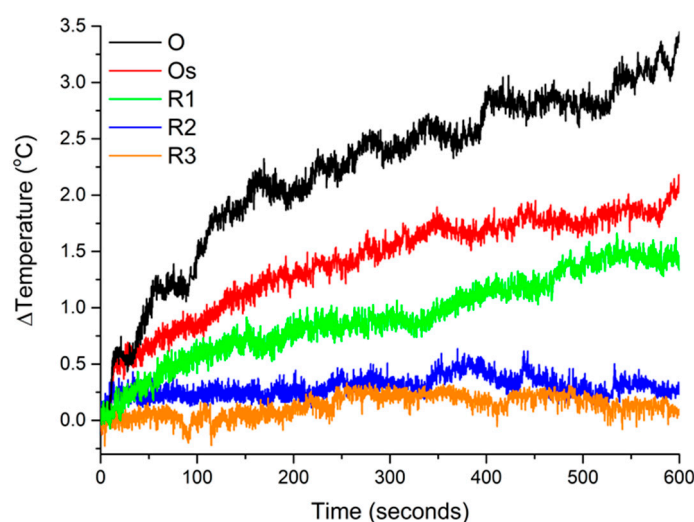
Figure 4. Magnetic hyperthermia activity of the various magnetic-plasmonic nanostructures all at a concentration of 0.2 mg/mL of Fe$_3$O$_4$.

4. Discussion

In this work, the following five stages of magnetic-plasmonic nanoparticles were studied: Fe$_3$O$_4$ nanoparticles (O), Fe$_3$O$_4$–Au core–satellite nanostructures (Os), Fe$_3$O$_4$–Au with thin gold shell (R1), Fe$_3$O$_4$–Au with intermediate thickness gold shell (R2), and Fe$_3$O$_4$–Au with thick gold shell (R3). These nanoparticle stages were studied in three applications—magnetophoresis, MRI or NMR contrasting, and magnetic hyperthermia.

The magnetophoresis rate of magnetic-based nanostructures is key in magnetic field-driven drug delivery, magnetic sorting, and other applications requiring magnetic manipulation. It was found that increased gold coating leads to a reduction in the magnetophoresis rate, rendering the nanoparticle less responsive to magnetic fields. The magnetophoresis speed is reduced to ca. 1% for the thickest gold shell compared to the uncoated iron oxide nanoparticle (see Table 1 for further details). The magnetophoresis speed decreases exponentially (see Figure 5) with increased gold shell thickness; thus, if responsivity is required for the application, a thinner gold coating is preferable. We attribute this reduced responsivity of the increased gold shell thickness to a reduced magnetic saturation, loss of cooperative behavior, and increased drag forces.
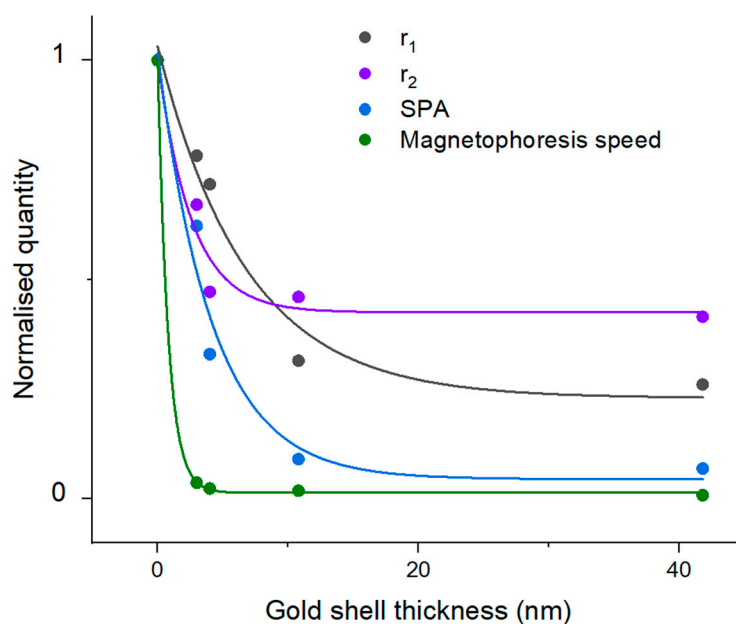
Figure 5. Exponential dependency of the normalized NMR relaxivities r_1 and r_2, the specific power absorption (SPA), and the magnetophoresis speed (v_{mag}) as a function of gold shell thickness. See Table 1 for values.

Iron oxide nanoparticles are commonly used as MRI contrast agents, specifically as T_2 agents. In this work, the T_1 and T_2 relaxivities (r_1 and r_2) of the various magnetic-plasmonic nanostructures were measured. As with the magnetophoresis, the T_1 and T_2 relaxivities, r_1 and r_2, decreased exponentially with additional gold growth (see Table 1). Compared to the purely magnetic counterpart, the thickest gold shell has a reduced relaxivity, to 22.2% and 41.6% for r_1 and r_2, respectively. These relaxivities also decreased exponentially (see Figure 5) with increased gold shell thickness (see Figure 5). We attribute this decreased relaxivity of thicker gold shells to reduced magnetic saturation, loss of cooperative behavior, and reduced exchange interaction with water nuclei.

Lastly, increasing the gold content of the magnetic-plasmonic hybrid nanoparticles led to an exponential decrease (see Figure 5) in the specific power absorption of the nanoparticles undergoing magnetic hyperthermia. A reduction to 14.3% was seen for the intrinsic loss power parameter, a measurement of heating efficiency that considers magnetic field strength and frequency, for the thickest gold shell on the magnetic core compared to the purely magnetic nanoparticle. This reduced heating efficiency with gold addition is likely a result of reduced cooperative behavior along with reduced magnetic saturation.

5. Conclusions

In conclusion, increasing the gold shell thickness has a significant reduction in the magnetophoresis rate, T_1 and T_2 contrast, and magnetic hyperthermia activity of iron oxide nanoparticles. A number

of factors are likely responsible for this reduced activity with increased gold shell thickness. We hypothesize that less cooperation due to reduced dipole–dipole magnetic interaction forces and a reduced magnetic saturation owing to the decreased magnetic volume and possible diamagnetic magnetic shielding by the gold shell are predominantly responsible.

In a previous work ([28]), we demonstrated that the thinner gold shells (R1 and R2) exhibit a large spectral drift between the optical absorption (highest photothermal activity) and the optical scattering (strongest optical imaging contrast). We demonstrate in this work that these thinner gold shells are also better for magnetic-based applications. Hence, this work further emphasizes that a thick gold shell is not necessary to achieve a highly functional nanotheranostic nanoplatform. In other words, thinner gold coating appears preferable in an extending series of both magnetic- and light-based applications.

References

1. Hu, X.; Tang, Y.; Hu, Y.; Lu, F.; Lu, X.; Wang, Y.; Li, J.; Li, Y.; Ji, Y.; Wang, W.; et al. Gadolinium-chelated conjugated polymer-based nanotheranostics for photoacoustic/magnetic resonance/NIR-II fluorescence imaging-guided cancer photothermal therapy. *Theranostics* **2019**, *9*, 4168–4181. [CrossRef] [PubMed]

2. Dadfar, S.M.; Roemhild, K.; Drude, N.I.; von Stillfried, S.; Knüchel, R.; Kiessling, F.; Lammers, T. Iron oxide nanoparticles: Diagnostic, therapeutic and theranostic applications. *Adv. Drug Deliv. Rev.* **2019**, *138*, 302–325. [CrossRef] [PubMed]

3. Knežević, N.; Kaluderović, G.N. Silicon-based nanotheranostics. *Nanoscale* **2017**, *9*, 12821–12829. [CrossRef] [PubMed]

4. Pedrosa, P.; Vinhas, R.; Fernandes, A.; Baptista, P.V. Gold nanotheranostics: Proof-of-concept or clinical tool? *Nanomaterials* **2015**, *5*, 1853–1879. [CrossRef]

5. Saini, A.; Maurer, T.; Lorenzo, I.I.; Santos, A.R.; Béal, J.; Goffard, J.; Gérard, D.; Vial, A.; Plain, J. Synthesis and SERS Application of SiO$_2$@Au Nanoparticles. *Plasmonics* **2015**, *10*, 791–796. [CrossRef]

6. Rastinehad, A.R.; Anastos, H.; Wajswol, E.; Winoker, J.S.; Sfakianos, J.P.; Doppalapudi, S.K.; Carrick, M.R.; Knauer, C.J.; Taouli, B.; Lewis, S.C.; et al. Gold nanoshell-localized photothermal ablation of prostate tumors in a clinical pilot device study. *Proc. Natl. Acad. Sci. USA* **2019**, *116*, 18590–18596. [CrossRef]

7. Imai, M.; Mine, K.; Tomonari, H.; Uchiyama, J.; Matuzaki, S.; Niko, Y.; Hadano, S.; Watanabe, S. Dark-Field Microscopic Detection of Bacteria using Bacteriophage-Immobilized SiO$_2$@AuNP Core-Shell Nanoparticles. *Anal. Chem.* **2019**, *91*, 12352–12357. [CrossRef]

8. Gossuin, Y.; Gillis, P.; Hocq, A.; Vuong, Q.L.; Roch, A. Magnetic resonance relaxation properties of superparamagnetic particles. *Wiley Interdiscip. Rev. Nanomed. Nanobiotechnol.* **2009**, *1*, 299–310. [CrossRef]

9. Shao, H.; Yoon, T.-J.; Liong, M.; Weissleder, R.; Lee, H. Magnetic nanoparticles for biomedical NMR-based diagnostics. *Beilstein J. Nanotechnol.* **2010**, *1*, 142–154. [CrossRef]

10. Price, P.M.; Mahmoud, W.E.; Al-Ghamdi, A.A.; Bronstein, L.M. Magnetic drug delivery: Where the field is going. *Front. Chem.* **2018**, *6*. [CrossRef]

11. Dukenbayev, K.; Korolkov, I.V.; Tishkevich, D.I.; Kozlovskiy, A.L.; Trukhanov, S.V.; Gorin, Y.G.; Shumskaya, E.E.; Kaniukov, E.Y.; Vinnik, D.A.; Zdorovets, M.V.; et al. Fe$_3$O$_4$ nanoparticles for complex targeted delivery and boron neutron capture therapy. *Nanomaterials* **2019**, *9*, 494. [CrossRef]

12. Salunkhe, A.B.; Khot, V.M.; Pawar, S.H. Magnetic Hyperthermia with Magnetic Nanoparticles: A Status Review. *Curr. Top. Med. Chem.* **2014**, *14*, 572–594. [CrossRef] [PubMed]

13. Thorat, N.D.; Tofail, S.A.M.; Von Rechenberg, B.; Townley, H.; Brennan, G.; Silien, C.; Yadav, H.M.; Steffen, T.; Bauer, J. Physically stimulated nanotheranostics for next generation cancer therapy: Focus on magnetic and light stimulations. *Appl. Phys. Rev.* **2019**, *6*, 041306. [CrossRef]

14. Zborowski, M.; Chalmers, J.J. Rare cell separation and analysis by magnetic sorting. *Anal. Chem.* **2011**, *83*, 8050–8056. [CrossRef] [PubMed]

15. Belyanina, I.; Kolovskaya, O.; Zamay, S.; Gargaun, A.; Zamay, T.; Kichkailo, A. Targeted magnetic nanotheranostics of cancer. *Molecules* **2017**, *22*, 975. [CrossRef] [PubMed]

16. Kim, D.; Jon, S. Gold nanoparticles in image-guided cancer therapy. *Inorg. Chim. Acta* **2012**, *393*, 154–164. [CrossRef]

17. Alvarez-Puebla, R.A.; Liz-Marzán, L.M. SERS-based diagnosis and biodetection. *Small* **2010**, *6*, 604–610. [CrossRef] [PubMed]

18. Panchapakesan, B.; Book-Newell, B.; Sethu, P.; Rao, M.; Irudayaraj, J. Gold nanoprobes for theranostics. *Nanomedicine* **2011**, *6*, 1787–1811. [CrossRef]

19. Artur, C.G.; Womack, T.; Zhao, F.; Eriksen, J.L.; Mayerich, D.; Shih, W.-C. Plasmonic nanoparticle-based expansion microscopy with surface-enhanced Raman and dark-field spectroscopic imaging. *Biomed. Opt. Express* **2018**, *9*, 603. [CrossRef]

20. Sokolov, K.; Follen, M.; Aaron, J.; Pavlova, I.; Malpica, A.; Lotan, R.; Richards-Kortum, R. Real-time vital optical imaging of precancer using anti-epidermal growth factor receptor antibodies conjugated to gold nanoparticles. *Cancer Res.* **2003**, *63*, 1999–2004.

21. Kuttner, C. Plasmonics in Sensing: From Colorimetry to SERS Analytics. In *Plasmonics*; IntechOpen: London, UK, 2018.

22. Duncan, B.; Kim, C.; Rotello, V.M. Gold nanoparticle platforms as drug and biomacromolecule delivery systems. *J. Control. Release* **2010**, *148*, 122–127. [CrossRef] [PubMed]

23. Huang, X.; Jain, P.K.; El-Sayed, I.H.; El-Sayed, M.A. Plasmonic photothermal therapy (PPTT) using gold nanoparticles. *Lasers Med. Sci.* **2008**, *23*, 217–228. [CrossRef] [PubMed]

24. Asharani, P.V.; Lianwu, Y.; Gong, Z.; Valiyaveettil, S. Comparison of the toxicity of silver, gold and platinum nanoparticles in developing zebrafish embryos. *Nanotoxicology* **2011**, *5*, 43–54. [CrossRef] [PubMed]

25. Dong, W.; Li, Y.; Niu, D.; Ma, Z.; Gu, J.; Chen, Y.; Zhao, W.; Liu, X.; Liu, C.; Shi, J. Facile synthesis of monodisperse superparamagnetic Fe_3O_4 Core@hybrid@Au shell nanocomposite for bimodal imaging and photothermal therapy. *Adv. Mater.* **2011**, *23*, 5392–5397. [CrossRef]

26. Esenturk, E.N.; Hight Walker, A.R. Gold nanostar @ iron oxide core–shell nanostructures: Synthesis, characterization, and demonstrated surface-enhanced Raman scattering properties. *J. Nanoparticle Res.* **2013**, *15*, 1364. [CrossRef]

27. JitKang Lim, B.; Eggeman, A.; Lanni, F.; Tilton, R.D.; Majetich, S.A.; Majetich, S.A.; Eggeman, A.; Lim, J.K.; Tilton, R.D.; Lanni, F. Synthesis and Single-Particle Optical Detection of Low-Polydispersity Plasmonic-Superparamagnetic Nanoparticles. *Adv. Mater* **2008**, *20*, 1721–1726. [CrossRef]

28. Brennan, G.; Thorat, N.D.; Pescio, M.; Bergamino, S.; Bauer, J.; Liu, N.; Tofail, S.A.M.; Silien, C. Spectral drifts in surface textured Fe_3O_4-Au, core–shell nanoparticles enhance spectra-selective photothermal heating and scatter imaging. *Nanoscale* **2020**, *12*, 12632–12638. [CrossRef]

29. Jain, P.K.; Xiao, Y.; Walsworth, R.; Cohen, A.E. Surface Plasmon Resonance Enhanced Magneto-Optics (SuPREMO): Faraday Rotation Enhancement in Gold-Coated Iron Oxide Nanocrystals. *Nano Lett.* **2009**, *9*, 1644–1650. [CrossRef]

30. Chen, K.-L.; Yeh, Y.-W.; Chen, J.-M.; Hong, Y.-J.; Huang, T.-L.; Deng, Z.-Y.; Wu, C.-H.; Liao, S.-H.; Wang, L.-M. Influence of magnetoplasmonic γ-Fe_2O_3/Au core/shell nanoparticles on low-field nuclear magnetic resonance. *Sci. Rep.* **2016**, *6*, 35477. [CrossRef] [PubMed]

31. Li, Y.; Liu, J.; Zhong, Y.; Zhang, J.; Wang, Z.; Wang, L.; An, Y.; Lin, M.; Gao, Z.; Zhang, D. Biocompatibility of Fe_3O_4@Au composite magnetic nanoparticles in vitro and in vivo. *Int. J. Nanomed.* **2011**, *6*, 2805–2819. [CrossRef] [PubMed]

32. Karakoçak, B.B.; Raliya, R.; Davis, J.T.; Chavalmane, S.; Wang, W.N.; Ravi, N.; Biswas, P. Biocompatibility of gold nanoparticles in retinal pigment epithelial cell line. *Toxicol. Vitr.* **2016**, *37*, 61–69. [CrossRef] [PubMed]

33. Hoshyar, N.; Gray, S.; Han, H.; Bao, G. The effect of nanoparticle size on in vivo pharmacokinetics and cellular interaction. *Nanomedicine* **2016**, *11*, 673–692. [CrossRef] [PubMed]

34. Davis, K.; Cole, B.; Ghelardini, M.; Powell, B.A.; Mefford, O.T. Quantitative Measurement of Ligand Exchange with Small-Molecule Ligands on Iron Oxide Nanoparticles via Radioanalytical Techniques. *Langmuir* **2016**, *32*, 13716–13727. [CrossRef] [PubMed]

35. Shen, M.; Cai, H.; Wang, X.; Cao, X.; Li, K.; Wang, S.H.; Guo, R.; Zheng, L.; Zhang, G.; Shi, X. Facile one-pot preparation, surface functionalization, and toxicity assay of APTS-coated iron oxide nanoparticles. *Nanotechnology* **2012**, 23. [CrossRef] [PubMed]

36. Duff, D.G.; Baiker, A.; Edwards, P.P. A new hydrosol of gold clusters. *J. Chem. Soc. Chem. Commun.* **1993**, *9*, 96–98. [CrossRef]

37. Oldenburg, S.J.; Averitt, R.D.; Westcott, S.L.; Halas, N.J. Nanoengineering of optical resonances. *Chem. Phys. Lett.* **1998**, *288*, 243–247. [CrossRef]

38. Herea, D.-D.; Danceanu, C.; Radu, E.; Labusca, L.; Lupu, N.; Chiriac, H. Comparative effects of magnetic and water-based hyperthermia treatments on human osteosarcoma cells. *Int. J. Nanomed.* **2018**, *13*, 5743–5751. [CrossRef]

39. Lim, J.K.; Yeap, S.P.; Leow, C.H.; Toh, P.Y.; Low, S.C. Magnetophoresis of iron oxide nanoparticles at low field gradient: The role of shape anisotropy. *J. Colloid Interface Sci.* **2014**, *421*, 170–177. [CrossRef]

40. Lyons, S.; Mc Kiernan, E.P.; Dee, G.; Brougham, D.F.; Morrin, A. Electrostatically modulated magnetophoretic transport of functionalised iron-oxide nanoparticles through hydrated networks. *Nanoscale* **2020**, *12*, 10550–10558. [CrossRef]

41. Lim, J.; Lanni, C.; Evarts, E.R.; Lanni, F.; Tilton, R.D.; Majetich, S.A. Magnetophoresis of nanoparticles. *ACS Nano* **2011**, *5*, 217–226. [CrossRef]

42. Lim, J.; Yeap, S.P.; Low, S.C. Challenges associated to magnetic separation of nanomaterials at low field gradient. *Sep. Purif. Technol.* **2014**, *123*, 171–174. [CrossRef]

43. Yeap, S.P.; Ahmad, A.L.; Ooi, B.S.; Lim, J. Electrosteric stabilization and its role in cooperative magnetophoresis of colloidal magnetic nanoparticles. *Langmuir* **2012**, *28*, 14878–14891. [CrossRef] [PubMed]

44. Bakhteeva, I.A.; Medvedeva, I.V.; Uimin, M.A.; Byzov, I.V.; Zhakov, S.V.; Yermakov, A.E.; Shchegoleva, N.N. Magnetic sedimentation and aggregation of $Fe_3O_4@SiO_2$ nanoparticles in water medium. *Sep. Purif. Technol.* **2016**, *159*, 35–42. [CrossRef]

45. Benelmekki, M.; Montras, A.; Martins, A.J.; Coutinho, P.J.G.; Martinez, L.M. Magnetophoresis behaviour at low gradient magnetic field and size control of nickel single core nanobeads. *J. Magn. Magn. Mater.* **2011**, *323*, 1945–1949. [CrossRef]

46. Moeser, G.D.; Roach, K.A.; Green, W.H.; Hatton, T.A.; Laibinis, P.E. High-gradient magnetic separation of coated magnetic nanoparticles. *AIChE J.* **2004**, *50*, 2835–2848. [CrossRef]

47. Gerbei, R.; Takayasu, M.; Friedlaender, F.J. Generalization of HGMS theory: The capture of ultra-fine particles. *IEEE Trans. Magn.* **1983**, *19*, 2115–2117. [CrossRef]

48. Yavuz, C.T.; Mayo, J.T.; Yu, W.W.; Prakash, A.; Falkner, J.C.; Yean, S.; Cong, L.; Shipley, H.J.; Kan, A.; Tomson, M.; et al. Low-field magnetic separation of monodisperse Fe_3O_4 nanocrystals. *Science* **2006**, *314*, 964–967. [CrossRef]

49. Faraudo, J.; Andreu, J.S.; Camacho, J. Understanding diluted dispersions of superparamagnetic particles under strong magnetic fields: A review of concepts, theory and simulations. *Soft Matter* **2013**, *9*, 6654–6664. [CrossRef]

50. Zahn, K.; Lenke, R.; Maret, G. Friction coefficient of rod-like chains of spheres at very low Reynolds numbers. I. Experiment. *J. Phys. II* **1994**, *4*, 555–560. [CrossRef]

51. Tamer, U.; Cetin, D.; Suludere, Z.; Boyaci, I.H.; Temiz, H.T.; Yegenoglu, H.; Daniel, P.; Dinçer, I.; Elerman, Y. Gold-coated iron composite nanospheres targeted the detection of Escherichia coli. *Int. J. Mol. Sci.* **2013**, *14*, 6223–6240. [CrossRef]

52. Dizaji, A.N.; Yilmaz, M.; Piskin, E. Silver or gold deposition onto magnetite nanoparticles by using plant extracts as reducing and stabilizing agents. *Artif. CellsNanomed. Biotechnol.* **2016**, *44*, 1109–1115. [CrossRef]

53. Xie, H.Y.; Zhen, R.; Wang, B.; Feng, Y.J.; Chen, P.; Hao, J. Fe_3O_4/Au core/shell nanoparticles modified with Ni2+-nitrilotriacetic acid specific to histidine-tagged proteins. *J. Phys. Chem. C* **2010**, *114*, 4825–4830. [CrossRef]

54. Tomitaka, A.; Ota, S.; Nishimoto, K.; Arami, H.; Takemura, Y.; Nair, M. Dynamic magnetic characterization and magnetic particle imaging enhancement of magnetic-gold core–shell nanoparticles. *Nanoscale* **2019**, *11*, 6489–6496. [CrossRef] [PubMed]

55. Han, Y.; Lei, S.L.; Lu, J.H.; He, Y.; Chen, Z.W.; Ren, L.; Zhou, X. Potential use of SERS-assisted theranostic strategy based on Fe_3O_4/Au cluster/shell nanocomposites for bio-detection, MRI, and magnetic hyperthermia. *Mater. Sci. Eng. C* **2016**, *64*, 199–207. [CrossRef] [PubMed]

56. Montazerabadi, A.R.; Oghabian, M.A.; Irajirad, R.; Muhammadnejad, S.; Ahmadvand, D.; Delavari, H.H.; Mahdavi, S.R. Development of Gold-Coated Magnetic Nanoparticles as a Potential MRI Contrast Agent. *Nano* **2015**, *10*, 1550048. [CrossRef]

57. Gangopadhyay, P.; Gallet, S.; Franz, E.; Persoons, A.; Verbiest, T. Novel superparamagnetic core(shell) nanoparticles for magnetic targeted drug delivery and hyperthermia treatment. *IEEE Trans. Magn.* **2005**, *41*, 4194–4196. [CrossRef]

58. Billen, A.; de Cattelle, A.; Jochum, J.K.; Van Bael, M.J.; Billen, J.; Seo, J.W.; Brullot, W.; Koeckelberghs, G.; Verbiest, T. Novel synthesis of superparamagnetic plasmonic core-shell iron oxide-gold nanoparticles. *Phys. B Condens. Matter* **2019**, *560*, 85–90. [CrossRef]

59. Hao, L.; Leng, Y.; Zeng, L.; Chen, X.; Chen, J.; Duan, H.; Huang, X.; Xiong, Y.; Chen, X. Core–Shell-Heterostructured Magnetic–Plasmonic Nanoassemblies with Highly Retained Magnetic–Plasmonic Activities for Ultrasensitive Bioanalysis in Complex Matrix. *Adv. Sci.* **2020**, 7. [CrossRef]

60. Song, Y.; Ding, J.; Wang, Y. Shell-dependent evolution of optical and magnetic properties of Co@Au core-shell nanoparticles. *J. Phys. Chem. C* **2012**, *116*, 11343–11350. [CrossRef]

61. Ammar, M.; Mazaleyrat, F.; Bonnet, J.P.; Audebert, P.; Brosseau, A.; Wang, G.; Champion, Y. Synthesis and characterization of core–shell structure silica-coated $Fe_{29.5}Ni_{70.5}$ nanoparticles. *Nanotechnology* **2007**, *18*, 285606. [CrossRef]

62. Banerjee, S.; Raja, S.O.; Sardar, M.; Gayathri, N.; Ghosh, B.; Dasgupta, A. Iron oxide nanoparticles coated with gold: Enhanced magnetic moment due to interfacial effects. *J. Appl. Phys.* **2011**, *109*, 123902. [CrossRef]

63. León-Félix, L.; Chaker, J.; Parise, M.; Coaquira, J.A.H.; De Los Santos Valladares, L.; Bustamante, A.; Garg, V.K.; Oliveira, A.C.; Morais, P.C. Synthesis and characterization of uncoated and gold-coated magnetite nanoparticles. *Hyperfine Interact.* **2014**, *224*, 179–188. [CrossRef]

64. Runge, V.M. Safety of the Gadolinium-Based Contrast Agents for Magnetic Resonance Imaging, Focusing in Part on Their Accumulation in the Brain and Especially the Dentate Nucleus. *Investig. Radiol.* **2016**, *51*, 273–279. [CrossRef] [PubMed]

65. Zhou, Z.; Zhao, Z.; Zhang, H.; Wang, Z.; Chen, X.; Wang, R.; Chen, Z.; Gao, J. Interplay between longitudinal and transverse contrasts in Fe_3O_4 nanoplates with (111) exposed surfaces. *ACS Nano* **2014**, *8*, 7976–7985. [CrossRef] [PubMed]

66. Roch, A.; Gossuin, Y.; Muller, R.N.; Gillis, P. Superparamagnetic colloid suspensions: Water magnetic relaxation and clustering. *J. Magn. Magn. Mater.* **2005**, *293*, 532–539. [CrossRef]

67. Zhang, W.; Liu, L.; Chen, H.; Hu, K.; Delahunty, I.; Gao, S.; Xie, J. Surface impact on nanoparticle-based magnetic resonance imaging contrast agents. *Theranostics* **2018**, *8*, 2521–2548. [CrossRef]

68. Marangoni, V.S.; Neumann, O.; Henderson, L.; Kaffes, C.C.; Zhang, H.; Zhang, R.; Bishnoi, S.; Ayala-Orozco, C.; Zucolotto, V.; Bankson, J.A.; et al. Enhancing T1 magnetic resonance imaging contrast with internalized gadolinium(III) in a multilayer nanoparticle. *Proc. Natl. Acad. Sci. USA* **2017**, *114*, 6960–6965. [CrossRef]

69. Pinho, S.L.C.; Pereira, G.A.; Voisin, P.; Kassem, J.; Bouchaud, V.; Etienne, L.; Peters, J.A.; Carlos, L.; Mornet, S.; Geraldes, C.F.G.C.; et al. Fine Tuning of the Relaxometry of γ-Fe_2O_3@SiO_2 Nanoparticles by Tweaking the Silica Coating Thickness. *ACS Nano* **2010**, *4*, 5339–5349. [CrossRef]

70. Joshi, H.M.; De, M.; Richter, F.; He, J.; Prasad, P.V.; Dravid, V.P. Effect of silica shell thickness of Fe_3O_4–SiO_x core–shell nanostructures on MRI contrast. *J. Nanoparticle Res.* **2013**, *15*, 1448. [CrossRef]

71. Ye, F.; Laurent, S.; Fornara, A.; Astolfi, L.; Qin, J.; Roch, A.; Martini, A.; Toprak, M.S.; Muller, R.N.; Muhammed, M. Uniform mesoporous silica coated iron oxide nanoparticles as a highly efficient, nontoxic MRI T2 contrast agent with tunable proton relaxivities. *Contrast Media Mol. Imaging* **2012**, *7*, 460–468. [CrossRef]

72. Park, J.A.; Lee, J.J.; Kim, I.S.; Park, B.H.; Lee, G.H.; Kim, T.J.; Ri, H.C.; Kim, H.J.; Chang, Y. Magnetic and MR relaxation properties of avidin-biotin conjugated superparamagnetic nanoparticles. *Colloids Surf. A Phys. Eng. Asp.* **2008**, *313*, 288–291. [CrossRef]

73. Peiris, P.M.; Schmidt, E.; Calabrese, M.; Karathanasis, E. Assembly of Linear Nano-Chains from Iron Oxide Nanospheres with Asymmetric Surface Chemistry. *PLoS ONE* **2011**, *6*, e15927. [CrossRef] [PubMed]

74. Carvalho, A.; Domingues, I.; Gonçalves, M.C. Core-shell superparamagnetic nanoparticles with interesting properties as contrast agents for MRI. *Mater. Chem. Phys.* **2015**, *168*, 42–49. [CrossRef]

75. Umut, E.; Pineider, F.; Arosio, P.; Sangregorio, C.; Corti, M.; Tabak, F.; Lascialfari, A.; Ghigna, P. Magnetic, optical and relaxometric properties of organically coated gold-magnetite (Au-Fe$_3$O$_4$) hybrid nanoparticles for potential use in biomedical applications. *J. Magn. Magn. Mater.* **2012**, *324*, 2373–2379. [CrossRef]

76. Lin, L.-S.; Yang, X.; Zhou, Z.; Yang, Z.; Jacobson, O.; Liu, Y.; Yang, A.; Niu, G.; Song, J.; Yang, H.H.; et al. Yolk–Shell Nanostructure: An Ideal Architecture to Achieve Harmonious Integration of Magnetic–Plasmonic Hybrid Theranostic Platform. *Adv. Mater.* **2017**, *29*, 1606681. [CrossRef]

77. Wust, P.; Hildebrandt, B.; Sreenivasa, G.; Rau, B.; Gellermann, J.; Riess, H.; Felix, R.; Schlag, P. Hyperthermia in combined treatment of cancer. *Lancet Oncol.* **2002**, *3*, 487–497. [CrossRef]

78. Saville, S.L.; Qi, B.; Baker, J.; Stone, R.; Camley, R.E.; Livesey, K.L.; Ye, L.; Crawford, T.M.; Thompson Mefford, O. The formation of linear aggregates in magnetic hyperthermia: Implications on specific absorption rate and magnetic anisotropy. *J. Colloid Interface Sci.* **2014**, *424*, 141–151. [CrossRef]

79. Das, H.; Debnath, N.; Arai, T.; Kawaguchi, T.; Sakamoto, N.; Shinozaki, K.; Suzuki, H.; Wakiya, N. Superparamagnetic magnesium ferrite/silica core-shell nanospheres: A controllable SiO$_2$ coating process for potential magnetic hyperthermia application. *Adv. Powder Technol.* **2019**, *30*, 3171–3181. [CrossRef]

80. Yu, X.; Zhu, Y. Preparation of magnetic mesoporous silica nanoparticles as a multifunctional platform for potential drug delivery and hyperthermia. *Sci. Technol. Adv. Mater.* **2016**, *17*, 229–238. [CrossRef]

81. Hu, Y.; Meng, L.; Niu, L.; Lu, Q. Facile synthesis of superparamagnetic Fe$_3$O$_4$@polyphosphazene@Au shells for magnetic resonance imaging and photothermal therapy. *Acs Appl. Mater. Interfaces* **2013**, *5*, 4586–4591. [CrossRef]

82. Lanier, O.L.; Korotych, O.I.; Monsalve, A.G.; Wable, D.; Savliwala, S.; Grooms, N.W.F.; Nacea, C.; Tuitt, O.R.; Dobson, J. Evaluation of magnetic nanoparticles for magnetic fluid hyperthermia. *Int. J. Hyperth.* **2019**, *36*, 687–701. [CrossRef] [PubMed]

Publisher's Note: MDPI stays neutral with regard to jurisdictional claims in published maps and institutional affiliations.